Boundary-updating as a source of history effect on decision uncertainty

Heeseung Lee[1] & Sang-Hun Lee[1,*]

[1]Department of Brain and Cognitive Sciences, Seoul National University, Seoul, Republic of Korea
[*]Corresponding author:
visionsl@snu.ac.kr
1 Gwanak-ro, Gwanak-gu, Seoul, Republic of Korea

Abstract

Boundary-updating, a process of updating decision boundaries, has been known to induce a history effect on binary choices. However, the history effect that boundary-updating has on decision uncertainty has been previously overlooked. Our study revealed that boundary-updating can also impact decision uncertainty, as evidenced by changes in response time, pupil-size, and dACC response, suggesting that boundary-updating is a source of history effect not only on choice but also decision uncertainty.

Stimulus and boundary are the two pillars of binary decision-making, both affecting observers' choices[1-9]. One pillar, the boundary, is often not presented explicitly at the time of decision and, thus, needs to be internally formed by observers based on previous experiences of the task[5-9]. This internal boundary tends to be continually updated towards previous stimuli[5-9] (**Fig. 1a-1**), inducing sequential dependence to binary choices. This boundary updating has accounted for a history effect on choice called 'repulsive bias,' where the current choice is biased away from previous stimuli on a trial-to-trial basis[6-10] (**Fig. 1a-3**).

Critically, this boundary-updating is supposed to confer a history effect also on 'decision uncertainty,' a cognitive quantity that increases as the stimulus and the boundary come nearer (**Fig. 1a-2**). Suppose the boundary was neutral, and a large stimulus was presented in the last trial (**Fig. 1a-3**, top and middle). The boundary would then move to the large side according to the boundary updating[5-9], bringing itself nearer to the stimuli associated with the 'large' choice but farther from those associated with the 'small' choice (**Fig. 1a-3**, bottom). Consequently, having previously viewed large stimuli, observers' 'large' choices will be accompanied by high uncertainty, whereas their 'small' choices by low uncertainty. Generally put, *the more congruent the current choice is with previous stimuli, the more uncertain it is*. We shall call this boundary-induced history effect on decision uncertainty 'pre-congruence effect.'

The pre-congruence effect is straightforward but has not been established empirically. The neglect of this obvious source of the variability in decision variability is odd, given the fundamental roles of decision uncertainty in adaptive human behavior such as volatility monitoring[11], learning from errors[12], and executive control[13], and its wide-ranging associations with behavioral (response time[14-17]), physiological (pupil-size[14,15]), and neural (salience network[11,14-16,18]) measures. Here, we probed human response time (RT), pupil size, and neural activity to ascertain the presence of the pre-congruence effect and assess its contribution to the variability in decision uncertainty.

We recruited 41 human participants and asked them to perform a binary classification task. The task involved classifying a series of rings presented in a pseudo-randomized order[19] as either 'small' or 'large,' one at a time, under moderate time pressure (**Fig. 1b**). As previously reported[5-9], the participants displayed the repulsive bias, making less of the 'large (small)' choice following the large (small) stimulus in the previous trial (**Fig. 1c**; $\beta_{S_{t-1}} = -0.57$ ($P = 2.87 \times 10^{-14}$), $\beta_{S_t} = 1.30$ ($P = 4.9 \times 10^{-22}$), $\beta_{C_{t-1}} =$

0.12 ($P = 0.036$), where S_{t-i}, stimulus on i-th preceding trial; C_{t-i}, choice on i-th preceding trial). Also, the repulsive bias was not constrained to the immediately preceding stimulus but extended to the stimulus at the lag of three trials (**Fig. 1d**).

To simulate how the boundary updating relates to the pre-congruence effect, we employed a Bayesian model for boundary updating (BMBU) (**Supplementary Fig. 1**). This model was previously developed by our group to capture the repulsive bias[9]. Before proceeding, we ensured that BMBU's choices readily captured the repulsive bias in the current data set, which is evident in the close correspondence of human and BMBU's psychometric functions (**Fig. 1c**) and regression coefficients (**Fig. 1d**). This implies that the participants update their internal boundary by shifting it toward previous stimuli as BMBU does. Then, we turned to the simulated decision uncertainty to see whether the boundary updating induces the pre-congruence effect. As we intuited early on (**Fig. 1a-3**), the more congruent BMBU's current choice is with previous stimuli, the more uncertain it is (**Fig. 1e**). BMBU also lets us foresee that the pre-congruence effect gradually diminishes as trials further lag (the purple bars in **Fig. 1f**). In addition to capturing this newly recognized history effect, BMBU also accounts for the well-established 'current-congruence effect'—a phenomenon where decision uncertainty decreases as the current choice becomes congruent with current stimuli[15,20,21] (as shown by the dotted, dashed, and solid lines in **Fig. 1e**; the yellow bar in **Fig. 1f**).

Moving on, as a first step to establish the presence of the pre-congruence effect, we probed RT (N=41), a well-known behavioral correlate of decision uncertainty[14-16]. As predicted, participants' RTs displayed both the pre-congruence effect ($\beta_{S_{t-1}*C_t} = 0.11$ ($P = 9.2 \times 10^{-9}$)) and the current-congruence effect ($\beta_{S_t*C_t} = -0.21$, ($P = 2.7 \times 10^{-18}$)) (**Fig. 2a-1**). Notably, the size of the pre-congruence effect was substantial and tantamount to 31% of that of the current-congruence effect (**Fig. 2b-1**). The pre-congruence effect on decision uncertainty could be traced back to three trials (**Fig. 2c-1**), which is consistent with the history effect on choices—the repulsive bias (**Fig. 1d**). We further confirmed the robustness of the pre-congruence and current-congruence effects using the RTs from another dataset (N=30), which were collected under different conditions, including trial-to-trial feedback, a shorter inter-trial interval (2.5 sec), and a larger number of stimuli (five) (**Supplementary Fig. 2**, $\beta_{S_{t-1}*C_t} = 0.050$ ($P = 7.6 \times 10^{-4}$), $\beta_{S_t*C_t} = -0.11$, ($P = 1.1 \times 10^{-6}$)).

Next, by regressing the fMRI data (N=18) onto BMBU's decision uncertainty, we identified the neural correlates of decision uncertainty in the dorsal anterior cingulate cortex (dACC) and insula (**Fig. 2e**; **Supplementary Table. 1**), consistent with previous studies[14,16,22]. At the time point with their highest correlation with BMBU's decision uncertainty (**Supplementary Fig. 3**), the dACC's responses showed the pre-congruence and current-congruence effects (**Fig. 2a-2**; $\beta_{S_{t-1}*C_t} = 0.053$, ($P = 0.0037$), $\beta_{S_t*C_t} = -0.076$ ($P = 0.0016$)). The pre-congruence effect in the dACC was equivalent in size to 46% of that of the current-congruence effect (**Fig. 2b-2**), traced back to two trials (**Fig. 2c-2**), and pronounced at the time points aligned with decision-making (**Fig. 2d-2**). In contrast, the insula exhibited only the current-congruence effect (**Fig. 2a3-d3**; $\beta_{S_{t-1}*C_t} = 0.028$ ($P = 0.083$), $\beta_{S_t*C_t} = -0.079$ ($P = 1.4 \times 10^{-5}$)).

Finally, the pupil-size data (N=23) also confirmed the pre-congruence effect. At the time point with its highest correlation with BMBU's decision uncertainty (**Supplementary Fig. 3**), the pupil size displayed both pre-congruence and current-congruence effects (**Fig. 2a-4**; $\beta_{S_{t-1}*C_t} = 0.053$ ($P = 0.0037$), $\beta_{S_t*C_t} = -0.076$ ($P = 0.0016$)). The pre-congruence effect in pupil size was equivalent in size to 35% of that of the current-congruence effect (**Fig. 2b-4**), traced back to the immediately preceding trial (**Fig. 2c-4**), and pronounced at the time points aligned with decision-making (**Fig. 2d-4**).

The pre-congruence effect demonstrated here differs considerably from earlier discoveries of the history effects on decision uncertainty. First, it differs from the history effect on RTs in tasks with an autocorrelated stimulus sequence[23] because the stimuli were independent across trials in our task[19]. Second, it differs from the 'priming effect[24,25],' where RTs become faster as current stimuli become similar to previous stimuli, an effect opposite to the pre-congruence effect, where RTs become slower under an identical situation. Third, it differs from the phenomenon where the congruence between subsequent choices biases RT[26] because the pre-congruence effect is founded on the congruence between previous stimuli and current choices, not between previous and current choices. Fourth, it differs from the so-called 'confidence leak[27],' where confidence reports are correlated across trials, because the confidence leak does not entail any historical effect on choices, whereas the pre-congruence effect entails the history effect on choice, the repulsive bias. Fifth, it differs from the so-called 'post-error slowing[28],' a tendency to slow down after committing an error on previous trials, because the pre-congruence effect does not need error feedback. Furthermore, the simulated decision uncertainty of BMBU does not show positive dependences between consecutive trials (**Supplementary Fig. 4**), which must be present both in the confidence leak and the post-error slowing. Lastly, our work should not be confused with the history effects on choices[15,17] which were investigated using RT, pupil-size, and confidence reports because they were not about decision uncertainty modulation but about choice bias.

Our work has important implications for the cognitive neuroscience of decision uncertainty and history effects. We could explain more of the trial-to-trial variability of decision uncertainty by discovering its historical source—the boundary updating. This will significantly facilitate discerning the 'genuine' neural substrate of decision uncertainty. For example, both dACC and insula appeared similarly involved in signaling task difficulty in previous studies[29]. However, we could point to dACC as a more genuine locus of decision uncertainty by demonstrating both pre-congruence and current-congruence effects in the dACC but only the current-congruence effect in the insula. In the same vein, we could no longer found any significant neural correlate of decision uncertainty without incorporating the boundary-updating for calculating decision uncertainty (**Supplementary Fig. 5**). Our discovery of the necessary involvement of the pre-congruence effect on decision uncertainty also calls for a need to reinterpret previous findings. For example, in metacognition research, the presence of history effects in confidence reports have been considered a source of metacognitive inefficiency[30]. According to the boundary updating, however, the absence, not the presence, of history effects in confidence reports may indicate metacognitive inefficiency.

Decision uncertainty is considered one of the core cognitive quantities that enable human intelligence[11-13,31]. Previous studies have been reporting diverse history effects on choices[10,17,32-34] but largely neglected the history effects on decision uncertainty. Our work points to a need to extend the current scope of studying the history effects further, including decision uncertainty, to understand the nature of human intelligence better.

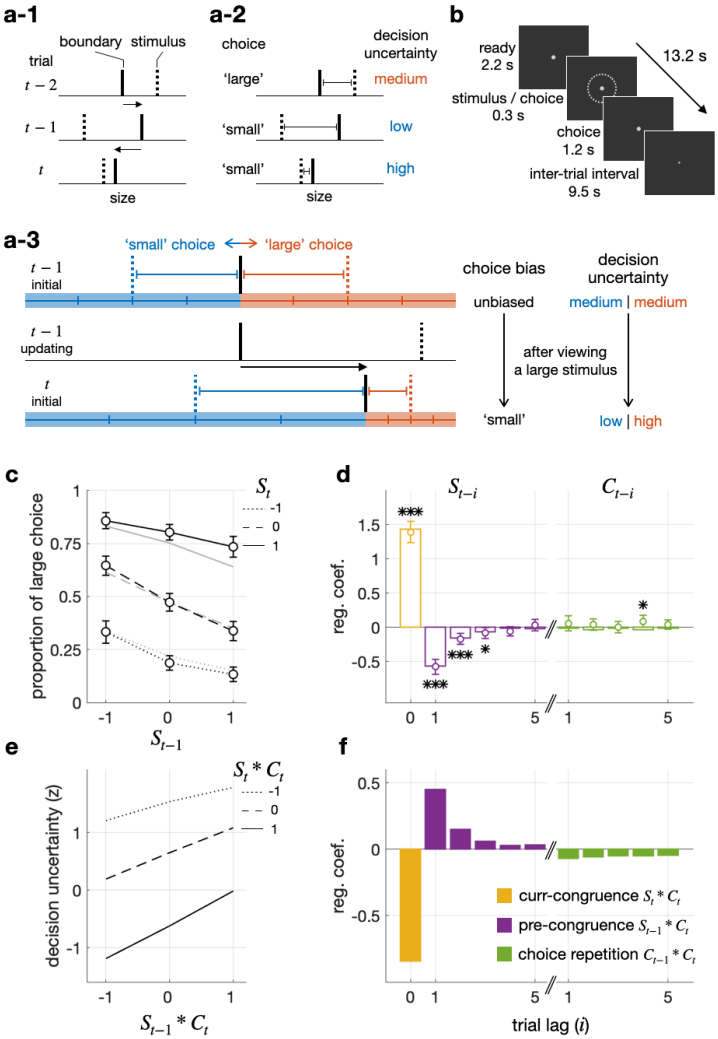

Figure 1 | The pre-congruence effect on decision uncertainty. a, Schematic illustration of boundary updating (**a-1**), decision uncertainty (**a-2**), and the pre-congruence effect in decision uncertainty (**a-3**). According to the boundary-updating account, the boundary (solid vertical black bars) is drawn towards previous stimuli (dotted vertical black bars) (**a-1**). Making a decision is more difficult as the boundary and the stimulus is closer (**a-2**). The boundary attraction to previous stimuli brings the pre-congruence effect to decision uncertainty (**a-3**). The horizontal baseline bar indicates the stimulus ranges that are smaller (blue) or larger (orange) than the boundary. The dotted blue and orange vertical bars indicate the average stimulus sizes smaller and larger than the boundary, respectively. The boundary is initially unbiased on the trial $t-1$ (**a-3**, top). As a result, distances from the boundary to the average stimulus sizes of 'large' and 'small' choices are equivalent. However, if a large stimulus was sampled on the trial $t-1$ (**a-3**, middle), then the boundary is biased to the large side at the trial t (**a-3**, bottom). As a result, the distance between the boundary and the average 'large' stimulus gets shorter, while the distance to the average 'small' stimulus becomes longer. This leads to an increase in decision uncertainty for 'large' choices and a decrease in decision uncertainty for 'small' choices after seeing a large stimulus in previous trials. **b,** Task structure. **c,d,** The repulsive bias demonstrated in psychometric curves (**c**) and logistic regressions (**d**). The proportion of 'large' choices are plotted against previous stimuli (S_{t-1}) conditioned on current stimuli (S_t) in black lines for humans and in gray for BMBU (**c**). The negative slopes of the curves indicate the repulsive bias. The coefficients in the multiple logistic regression of current choices (C_t) onto current and previous stimuli (S_{t-i}) and previous choices (C_{t-i}) are plotted in circles and bars for humans and BMBU, respectively (**d**). The significant coefficients of previous stimuli, not previous choices, indicate the repulsive bias. **e,f,** The pre- and the curr-congruence effects in decision uncertainty that are simulated by BMBM, shown in psychometric curves (**e**) and linear regressions (**f**) based on simulated choices. The simulated decision uncertainty increases with the congruence between current choices and previous stimuli ($S_{t-1} * C_t$) but decreases with the congruence between current choices and current stimuli ($S_t * C_t$), the former and latter implying the pre- and the curr-congruence effects on decision uncertainty, respectively (**e**). The coefficients in the multiple linear regression of the simulated decision uncertainty onto the congruences of current choices with previous stimuli ($S_{t-i} * C_t$) and with previous choices ($C_{t-i} * C_t$) (**f**). The pronounced coefficients of the congruence between current choices and past stimuli (purple bars) implies the pre-congruence effect. Here and thereafter, error bars indicate 95% confidence interval of the means, and asterisks indicate P values of two-sided Student's t-test: $*< 0.05$, $**< 0.01$, $***< 0.001$.

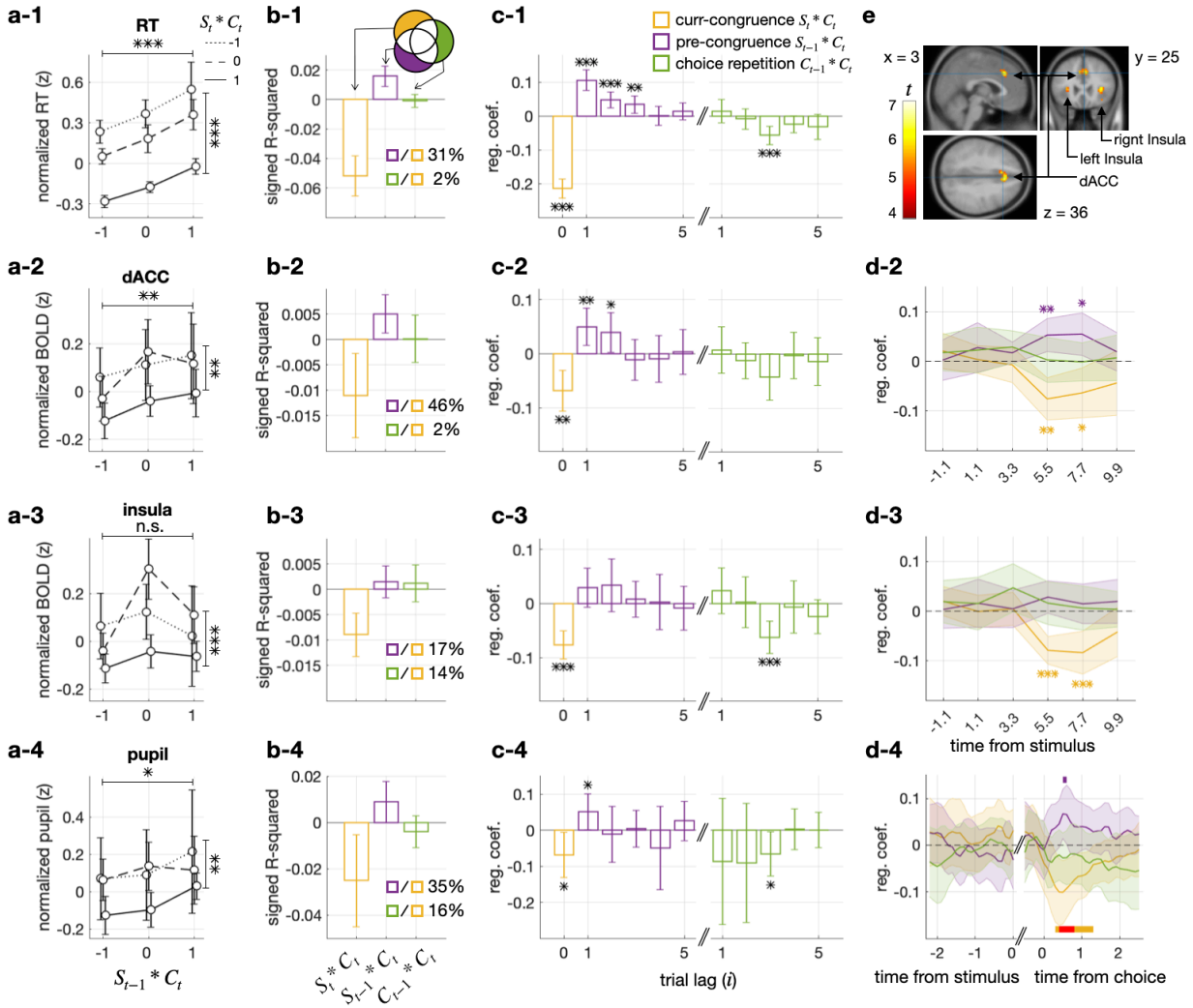

Figure 2 | The pre- and the curr-congruence effects on RT, cortical activity, and pupil-size. a, The pre- and the curr-congruence effects captured in chronometric (**1**), neurometric (**2**,**3**), and pupillometric (**4**) curves. Normalized measures of RT (**1**), dACC (**2**) and insula (**3**) BOLD signals acquired at the fourth time frame within a trial, and pupil-size (**4**) taken at 0.5 sec after button press are plotted against the congruences between current choices and immediately preceding stimuli ($S_{t-1} * C_t$) and the congruences between current choices and current stimuli ($S_t * C_t$). In each panel, the asterisks on top and side indicate the significant contributions of the pre-congruence effect ($S_{t-1} * C_t$) and the curr-congruence effect ($S_t * C_t$) to the measures of interest, respectively. Their significant contributions are ascertained by the multiple regressions of the measures of interest onto $S_{t-1} * C_t$, $S_t * C_t$, and $C_{t-1} * C_t$. The presence of the asterisks on top and side indicate that the RT, dACC activity, and pupil-size are under the influences of both the pre- and the curr-congruence effects, whereas the insula activity is under the influence of only the curr-congruence effect. **b,** Variances uniquely explained by the congruences of current choices with current stimuli (yellow), with immediately preceding stimuli (purple), and with immediately preceding choices (green). The percentages quantify the ratio of the explained variance sizes between the yellow bar and each of the others. **c,** The pre- and the curr-congruence effects and the effect of previous choices captured in multiple regression analyses. The coefficients in the multiple linear regression of the measures onto the congruences of current choices with current stimuli (yellow), past stimuli (purple), and past choices (green) are plotted in bars. The asterisks indicate the significant contributions of a given regressor to the variability of the measures. Note that the significant influence of the pre-congruence effect ($S_{t-i} * C_t$) for the RT (**1**), dACC activity (**2**), and pupil-size (**4**), but not for the insula activity (**3**). **d,** Time courses of the coefficients in the multiple regression of the dACC (**2**) and insula activity (**3**), and pupil-size (**4**) onto the congruences of current choices with current stimuli (yellow; $S_t * C_t$), with immediately preceding stimuli (purple; $S_{t-1} * C_t$), and with immediately preceding choices (green; $C_{t-1} * C_t$). The colored horizontal bars indicate *P* values of two-sided Student's *t*-test of the coefficients (purple and yellow: $*< 0.05$; red: $**< 0.01$) (**4**). The emergence of the pre-congruence effect is aligned with the time frames associated with decision-making for both dACC and pupil-size. **e,** *t*-statistics of voxel clusters whose BOLD signals significantly predict the simulated decision uncertainty (two-sided Student's *t*-test $P < 0.05$ after controlling the false discovery rate; the minimum number of contiguous voxels is 15).

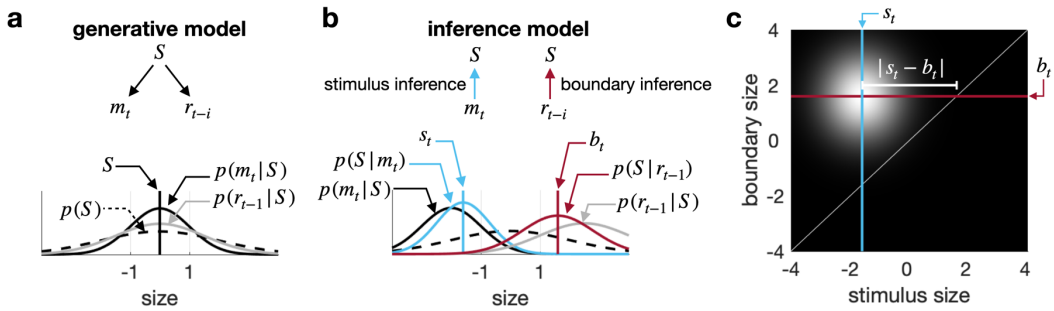

Supplementary Figure 1 | A Bayesian model of boundary-updating (BMBU). a, BMBU postulates that the current sensory measurement (m_t) of a stimulus and the memory measurement of the previous stimulus on the i-th preceding trial (r_{t-i}) are both randomly generated from normal distributions, namely $p(m_t|S_t)$ and $p(r_{t-i}|S_{t-i})$, respectively. For the purpose of illustration, we assume that $i = 1$ and $S_t = S_{t-i} = S$. Additionally, BMBU possesses prior knowledge of the distribution of physical stimulus size, denoted by the dashed curve $p(S)$. To account for the decay in memory precision observed in biological observers, BMBU widens the memory measurement noise, as represented by the width of the gray solid curve, relative to the sensory measurement noise, represented by the width of the black solid curve. **b,** BMBU calculates the current stimulus and the boundary by constructing posterior distributions of the stimulus size based on sensory measurements ($p(S|m_t)$) and memory measurements ($p(S|r_{t-1}, r_{t-2}, \dots)$), respectively. The estimates of the stimulus (indicated by the blue vertical line) and boundary (indicated by the red vertical line) are determined by the means of their respective posterior distributions. For the purposes of illustration, we only consider the memory measurement of the stimulus immediately preceding (r_{t-1}). It is worth noting that the boundary estimate (b_t) is biased toward the likelihoods of previous stimuli ($p(r_{t-i}|S)$), which explains the attractive bias of the boundary towards previous stimuli. **c,** The bivariate space displays the posterior distributions of both the boundary and stimulus, with the intensity indicating the probability density of the product of the two posterior distributions ($p(S \mid m_t) \times p(S|r_{t-1}, r_{t-2}, \dots)$). BMBU categorizes the current stimulus as 'large' if s_t is greater than b_t, and 'small' if it is smaller. In this particular example, the current choice would be 'small'. Decision uncertainty is quantified as the probability of the current choice being incorrect, and this probability decreases as the distance between the stimulus estimate and boundary estimate ($|s_t - b_t|$) increases.

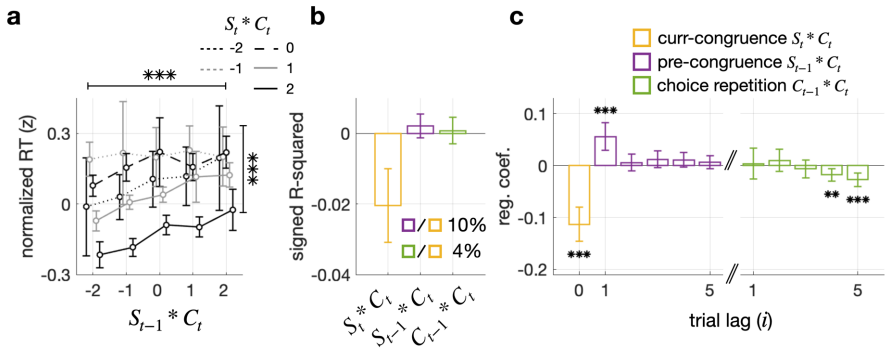

Supplementary Figure 2 | the pre- and current-congruence effects on reaction time (RT) in another task condition with trial-to-trial feedback, five stimuli, and a short inter-trial interval. a, RT is plotted against the congruences between current choices and the immediately preceding stimuli ($S_{t-1} * C_t$) and the congruences between current choices and current stimuli ($S_t * C_t$). The significance of the multiple regression coefficients for predicting RT by $S_{t-1} * C_t$, $S_t * C_t$, and $C_{t-1} * C_t$ are indicated by asterisks. The horizontal and vertical lines indicate the significance of the regression coefficients of $S_{t-1} * C_t$ and $S_t * C_t$, respectively. The pre-congruence effect is statistically significant in RT. **b,** the proportions of variance that are uniquely explained by the congruences of current choices to current stimuli (yellow), to immediately preceding stimuli (purple), and to immediately preceding choices (green). The percentages indicate the ratio between the sizes of the uniquely explained variances. **c,** the multiple regression coefficients of the congruences of current choices to current stimuli (yellow), previous stimuli (purple), and previous choices (green) for predicting RT.

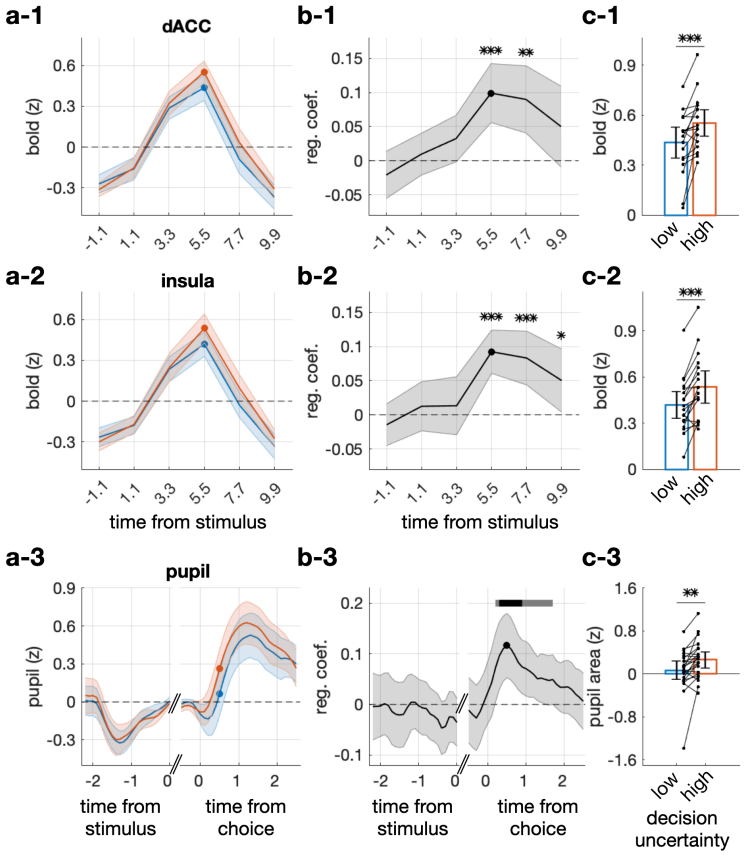

Supplementary Figure 3 | the time courses of dACC, insula, and pupil-size and their linear regressions to decision uncertainty. a, the time courses of (1) dACC, (2) insula, and (3) pupil-size, which were conditioned by the simulated decision uncertainty into lower (blue) and higher (red) decision uncertainty conditions. **b,** the linear regression coefficient of the simulated decision uncertainty to predict dACC, insula or pupil-size for each time frame. The *P* values of two-sided Student's *t*-test of the coefficients are indicated by the horizontal bar (gray: $*< 0.05$; black: $**< 0.01$). **c,** the BOLD signals and pupil-sizes are shown for the time frame with the most significant coefficient, which is indicated by the circles in the time courses (panels **a** and **b**). Each dot pair and line represent a single participant.

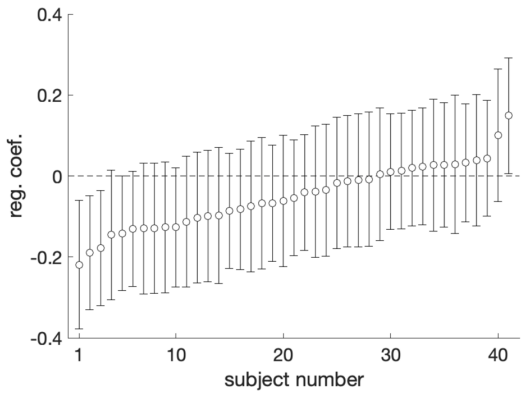

Supplementary Figure 4 | The regression coefficient between consecutive decision uncertainties. The circles represent the linear regression coefficients of the decision uncertainty of the previous trial used to predict the decision uncertainty of the current trial. The decision uncertainty was simulated using BMBU. Only a single participant showed a significantly positive correlation between consecutive decision uncertainties

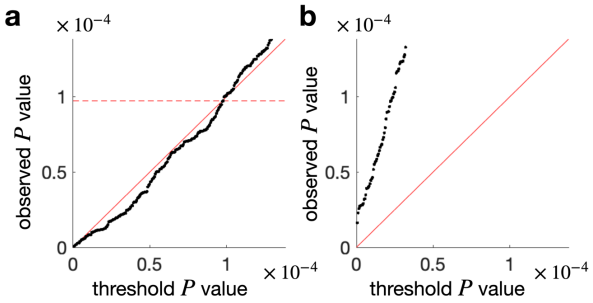

Supplementary Figure 5 | Controlling the false discovery rate (FDR) of the *P* values of the whole-brain analysis. a,b, The lowest P values of each voxel in the whole brain for predicting decision uncertainty in BMBU (**a**) and the constant-boundary model (**b**), respectively, plotted against the FDR threshold *P* values. The critical *P* value, which is the maximum *P* value lower than the FDR threshold (indicated by the horizontal dashed line), determines the significant voxels after controlling for FDR. For BMBU, 177 voxels were significant, whereas no voxel was significant for the constant-boundary model.

cortical area	contiguous voxel (N)	peak voxel		
		MNI coordinate	t	P
dorsal anterior cingulate cortex	64	[6, 27, 36]	6.29	8.2×10^{-6}
left insula	27	[-30, 21, 9]	6.5	5.7×10^{-6}
right insula	66	[36, 18, 6]	7.6	7.5×10^{-7}

Supplementary Table 1 | The brain regions where there was a significant correlation between BOLD signals and simulated decision uncertainty. We defined these regions based on two conditions: (1) the regression coefficient between the simulated decision uncertainty and the BOLD signal was significant (two-sided Student's t-test $P < 0.05$, after controlling the false discovery rate), and (2) there were at least 15 contiguous voxels that met the first condition.

Method

Behavior data acquisition

In the main results, we utilized two previously published datasets from our lab[9,35,36]The fMRI dataset[9] consisted of 18 participants (9 females) aged 20-30 years, while the eye tracking dataset[35,36] comprised 23 participants (11 females) aged 18-36 years. For the supplementary results, we used another dataset from our lab[37] that included 30 participants (13 females) aged 18-30 years. The experimental procedures were approved by the Research Ethics Committee of Seoul National University, and all participants provided informed consent and were unaware of the study's objectives.

Task procedure

The main data set used the following task procedure (**Fig. 1b**): Participants were instructed to fixate at the center of the screen and classify a brief (0.3s) ring-shaped stimulus as either 'small' or 'large' within 1.5s after stimulus onset by pressing the left or right key, respectively. The timing and identity of each key press were recorded. Trials were separated by 13.2s and participants were given feedback on their performance after each run of 26 trials.

Before the main runs, participants completed 54 practice trials followed by 180 threshold-calibration trials. During the threshold-calibration trials, which were separated by 2.7s, participants received trial-to-trial feedback based on the boundary with a radius of 2.84°. A Weibull function was fit to the psychometric curves obtained from the threshold-calibration trials using a maximum-likelihood procedure. The size threshold Δ° (i.e., the size difference between medium ring and large or small ring) associated with a 70.7% correct proportion was estimated from the fitted Weibull function. The mean and standard deviation of the estimated size threshold were 0.023 and 0.0078, respectively. One of three estimated ring sizes ($2.84 - \Delta°, 2.84°, 2.84 + \Delta°$) was shown on each trial. Participants had extensive training on the task before participating in the main experiments.

The supplementary data set involved participants performing the same classification task over 5 daily sessions with 1,700 trials using ring stimuli of 5 different sizes ($3.84°, 3.92°, 4.00°, 4.08°, 4.16°$), with trial-to-trial feedback and an inter-trial interval of 2.5s.

A Bayesian model for boundary-updating (BMBU)

The generative model. The generative model is the observers' causal account for noisy sensory measurements. Specifically, the true size of the ring, S, is the cause of a noisy measurement, m_t, on the current trial. This measurement becomes noisier as more trials pass, resulting in a noisier measurement of the value of S on trial $t - i$, which is denoted as r_{t-i} (**Supplementary Fig. 1**). The generative model can be defined using three probabilistic terms: the prior probability of S, $p(S)$, the likelihood of S given m_t, $p(m_t|S)$, and the likelihood of S given r_{t-i}, $p(r_{t-i}|S)$. All three terms are modeled as normal distribution functions, which are characterized by mean and standard deviation parameters, μ and σ. Specifically, the prior is characterized by μ_0 and σ_0, the likelihood for m_t is characterized by μ_{m_t} and σ_{m_t}, and the likelihood for r_{t-i} is characterized by $\mu_{r_{t-i}}$ and $\sigma_{r_{t-i}}$. The mean parameters of the likelihood functions are identical to the observed sensory measurements, m_t and r_{t-i}. Therefore, the four parameters that need to be learned are μ_0, σ_0, σ_{m_t}, and $\sigma_{r_{t-i}}$. The parameter σ_{m_t} is assumed to be constant across different values of m_t and across trials and is therefore reduced to a constant value σ_m. The parameter $\sigma_{r_{t-i}}$ is assumed to increase with the number of elapsed trials, and it is modeled as a parametric function of κ, where $\kappa > 0$: $\sigma_{r_{t-i}} = \sigma_m(1 + \kappa)^i$. As a result, the generative model is fully specified by the four parameters, which are represented as $\Theta = [\mu_0, \sigma_0, \sigma_m, \kappa]$.

Stimulus inference (s). To estimate the value of S on a current trial based on the sensory measurement m_t, a Bayesian approach was employed, where the mean of the posterior distribution of S given m_t, denoted as $p(S|m_t)$, was considered as the Bayesian estimate s_t. This posterior distribution is a conjugate normal distribution of the prior and the likelihood of S given the sensory evidence m_t. The Bayesian estimate s_t and its standard deviation σ_{s_t} were calculated as follows:

$$s_t = \frac{\sigma_0^2 m_t + \sigma_m^2 \mu_0}{\sigma_0^2 + \sigma_m^2};\ \sigma_{s_t} = \frac{\sigma_0 \sigma_m}{\sqrt{\sigma_0^2 + \sigma_m^2}}.$$

Class boundary inference (b). The Bayesian observer estimates the value of the class boundary on a current trial, b_t, by taking the mean of the posterior function based on a given set of retrieved sensory measurements, $\vec{r}_t = [r_{t-1}, r_{t-2}, \dots r_{t-n}]$: $(S|\vec{r}_t)$, The maximum number of measurements that can be retrieved, n, is set to 7 because it is much longer than the effective trial lags of the previous stimulus effect (**Fig. 1**). The posterior function, $p(S|\vec{r}_t)$, is a conjugate normal distribution of the prior and likelihoods of S given the evidence $\vec{r}_t$:

$$\begin{aligned} p(S|\vec{r}_t) &\propto p(\vec{r}_t|S)p(S) \\ &= p(r_{t-1}|S)p(r_{t-2}|S) \dots p(r_{t-7}|S)p(S) \end{aligned}$$

, whose mean and standard deviation were calculated based on the knowledge of how the retrieved stimulus becomes noisier as trials elapse:

$$b_t = \beta_0 \mu_0 + \sum_{i=1}^{7} \beta_i r_{t-i};\ \sigma_{b_t} = \sqrt{\beta_0^2 \sigma_0^2 + \sum_{i=1}^{7} \beta_i^2 \sigma_{r_{t-i}}^2}$$

, where $\beta_0 = \frac{\sigma_0^{-2}}{\sigma_0^{-2} + \sum_{i=1}^{7} \sigma_{r_{t-i}}^{-2}}$ and $\beta_i = \frac{\sigma_{r_{t-i}}^{-2}}{\sigma_0^{-2} + \sum_{i=1}^{7} \sigma_{r_{t-i}}^{-2}}$.

Deduction of choice (c) and decision uncertainty (u). For each trial, if s_t exceeds b_t, the simulated choice c_t is recorded as 'large' (or 1); otherwise, it is recorded as 'small' (or -1). In addition, we defined the decision uncertainty, u_t, which represents the likelihood that the current decision will be incorrect. Specifically, u_t is calculated as follows:

$$u_t = \Phi\left[\frac{-|s_t - b_t|}{\sqrt{\sigma_{s_t}^2 + \sigma_{b_t}^2}}\right],$$

where Φ stands for the standard normal cumulative function.

A constant-boundary model

The constant-boundary model comprises two parameters, the bias of the class boundary, μ_0, and the measurement noise, σ_m. In this model, we assumed that stimulus estimates, s_t, were sampled from a normal distribution, $\mathcal{N}(S_t, \sigma_m)$, where S_t represents the physical size of the stimulus. The uncertainty in each stimulus sample was assumed to be equal to σ_m, that is, $\sigma_{s_t} = \sigma_m$. Furthermore, we assumed that the boundary estimate, b_t, was a constant value, μ_0, with $\sigma_{b_t} = 0$.

Model fitting

To estimate the parameters of the generative model for each human participant, we used maximum likelihood estimation. Specifically, we sought to find the values of $\Theta = [\mu_0, \sigma_0, \sigma_m, \kappa]$ that maximized the sum of log-likelihoods across T individual choices made by the human observer, $\vec{C_T} = [C_1, C_2, \dots, C_T]$:

$$\widehat{\Theta} = \arg\max_{\Theta} \sum_{t=1}^{T} \log p(C_t|\Theta).$$

For each participant, we estimated the parameters of the generative model in the following steps. Initially, we used a MATLAB function, fminseachbnd, to find local minima of parameters with the iterative evaluation number set to 50. To acquire a set of candidate parameter estimates, we repeated this step by choosing 1,000 different initial parameter sets randomly sampled within uniform prior bounds. In the second step, we selected the top 20 candidate sets based on goodness-of-fit (sum of log-likelihoods) and searched for the minima using each of those 20 sets as initial parameters. We increased the iterative evaluation number to 100,000 and set tolerances of function and parameters to 10^{-7} for reliable estimation. Using the parameters fitted via the second step, we repeated the second step once more. Then, we selected the parameter set that showed the largest sum of likelihoods as the final parameter estimates. We excluded the first trial of each run and trials with reaction times less than 0.3 seconds from further analyses. This exclusion is necessary because the first trial of each run does not have its previous trial, which is necessary for investigating the repulsive influence. Additionally, a response made during the stimulus's initial presentation (0~0.3s) may be too hasty to reflect a normal cognitive decision-making process.

Estimation of decision uncertainty

By fitting the model parameters ($\widehat{\Theta} = [\hat{\mu}_0, \hat{\sigma}_0, \hat{\sigma}_m, \hat{\kappa}]$) separately for each human participant, we were able to create a Bayesian observer tailored to each individual. By conducting the experiment again with these Bayesian observers using the same stimulus sequences presented to their human counterparts, we obtained a sufficient number (10^6 repetitions) of simulated choices, c_t, and decision uncertainty values, u_t. These values were determined based on the corresponding number of stimulus estimates, s_t, and boundary estimates, b_t, for each Bayesian observer. Finally, we took the averages across those 10^6 simulations as the final outcomes. When estimating u_t for the observed choice C_t, we only included simulation outcomes where the simulated choice c_t matched the observed choice C_t.

Definition of congruence

The term 'congruence' refers to the product of the variable of interest and the current choice, where choices were represented as 1 for 'large' and -1 for 'small' and stimuli were represented as 1, 0, and -1 for large, medium, and small sizes, respectively. For instance, if the current choice was 'large (1)' and the previous stimulus was a 'small' size (-1), then the congruence would be -1 (1 * -1). In the supplementary data where there were five stimuli, the stimuli were encoded as [-2, -1, 0, 1, 2].

Definition of the signed R-squared

The signed R-squared is a measure that takes into account the direction of the relationship between a variable of interest and other variables in a multiple regression model. It is calculated by multiplying the sign of the regression coefficient with the uniquely explained variance of the variable. The uniquely explained variance is obtained through variance partitioning analysis[38,39], which involves comparing the R-squared values of the full regression model that includes all variables and the reduced regression model that excludes the variable of interest. For instance, to calculate the signed R-squared of variable x, we first calculate the R-squared of the full model (R^2_{xyz}) that includes variables x, y, and z. Next, we compute the R-squared of the reduced model (R^2_{yz}) that includes variables y and z only. The uniquely

explained variance of x ($R^2_{x,yz}$) is obtained by subtracting R^2_{yz} from R^2_{xyz}. Finally, the signed R-squared of x is defined as $sign(\beta_x)R^2_{x,yz}$, where $sign(\beta_x)$ is the sign of the regression coefficient β_x of the multiple regression model with variables x, y, and z as regressors.

BOLD signal

MRI data were collected using a 3 Tesla Siemens Tim Trio scanner equipped with a 12-channel Head Matrix coil at the Seoul National University Brain Imaging Center. Stimuli were generated using MATLAB (MathWorks) in conjunction with MGL (http://justingardner.net/mgl) on a Macintosh computer. Observers looked through an angled mirror attached to the head coil to view stimuli displayed via an LCD projector (Canon XEED SX60) onto a back-projection screen at the end of the magnet bore at a viewing distance of 87cm, yielding a field of view of 22×17°.

For each observer, we acquired three types of MRI images, as follows: (1) 3D, T1-weighted, whole-brain images (MPRAGE; resolution, 1×1×1mm; field of view (FOV), 256mm; repetition time (TR), 1.9s; time for inversion, 700ms; time to echo (TE), 2.36; and flip angle (FA), 9°), (2) 2D, T1-weighted, in-plane images (MPRAGE; resolution, 1.08×1.08×3.3mm; TR, 1.5s; T1, 700ms; TE, 2.79ms; and FA, 9°), and (3) 2D, T2*-weighted, functional images (gradient EPI; TR, 2.2s; TE, 40ms; FA, 73º; FOV, 208mm; image matrix, 90×90; slice thickness, 3mm with 10% space gap; slice, 32 oblique transfers slices; bandwidth, 790Hz/ps; and effective voxel size, 3.25×3.25×3.3mm).

The images of individual observers were normalized to the MNI template using the following steps: motion correction, coregistration to whole-brain anatomical images via the in-plane images[40], spike elimination, slice timing correction, normalization using the SPM DARTEL Toolbox[41] to 3×3×3mm voxel size, and smoothing with 8×8×8mm full-width half-maximum Gaussian kernel. All the procedures were implemented with SPM8 and SPM12 (http://www.fil.ion.ucl.ac.uk.spm) [42,43], except for spike elimination for which we used the AFNI toolbox [44]. The first six frames of each functional scan (the first trial of each run) were discarded to allow hemodynamic responses to reach a steady state. Then, the normalized BOLD time series at each voxel, each run, and each subject were preprocessed using linear detrending and high-pass filtering (132s cut-off frequency with a Butterworth filter), conversion into percent-change signals, correction for non-neural nuisance signals by regressing out the mean BOLD activity of the cerebrospinal fluid (CSF), and standardization by subtracting the mean activity and by dividing the standard deviation.

To define the anatomical mask of CSF, probability tissue maps for individual participants were generated from T1-weighted images, normalized to the MNI space, and smoothed as were done for the functional images by using SPM12, and then averaged across participants. Finally, the location of CSF was defined as respective groups of voxels in which the probability was more than 0.5.

Unfortunately, in a few of the sessions, functional images did not cover the entire brain. We investigated a brain region only when it does not loss any session. As a result, some voxels in the temporal pole, ventral orbitofrontal, and posterior cerebellum were excluded from data analysis.

To explore the brain regions that showed a correlation between BOLD signals and u_t, we conducted a regression analysis for each participant and voxel. The response variable for the regression model was the preprocessed BOLD signals concatenated across runs. We used three explanatory vectors in the regression model. The first vector was created by convolving the canonical hemodynamic function with u_t for each trial. The second vector was created by convolving the canonical hemodynamic function with a constant value of 1, and both vectors were standardized. The third vector contained only a single value of 1. The first regression coefficient indicated how well u_t predicted the BOLD signal for each voxel, and by calculating this coefficient for every voxel, we generated a map of regression coefficients for each participant and the entire brain.

To determine whether the average coefficient of u_t across participants significant, we performed a two-sided Student *t*-test on each voxel. We then corrected the *P* values of the entire brain for false discovery rate (FDR)[45] (**Supplementary Fig. 5**). The total number of voxels in the entire brain was

90,481, and we defined the brain areas significantly correlated with u_t as the voxel clusters covering a region larger than 15 contiguous voxels and having FDR-corrected P values less than 0.05. For the ROI analysis, we averaged the preprocessed BOLD signals across individual voxels within an ROI.

Pupillometry

Stimuli were presented in a dimly lit room on a gamma-linearized 22-inch CRT monitor (Totoku CV921X CRT monitor) operating at vertical refresh rate of 180Hz and a spatial resolution of 800×600 pixels. Stimuli were generated using MATLAB (MathWorks) in conjunction with MGL (http://justingardner.net/mgl) on a Macintosh computer. Observers viewed the monitor at a distance of 90cm while their binocular eye positions were sampled at 500Hz by an infrared eye tracker (EyeLink 1000 Desktop Mount, SR Research; instrument noise, 0.01° RMS). The LED illuminator and camera were positioned side by side, at a distance of 65cm from the observer, and angled toward the observer's face to ensure that infrared light illuminated both eyes and was being reflected from both eyes and imaged on the camera sensor.

When measuring gaze position using video-based methods, eye blinks can interfere with the accuracy of the data, as pupil and gaze information are not available during these periods. We identified eye blinks based on three criteria: (i) missing pupil data for either eye, (ii) pupil-size measurements with unrealistically large fluctuations (>50 units per sample), or (iii) substantial deviation (>20°) of gaze position from the screen center. Data collected immediately before and after an eye blink (±200 ms) were likely contaminated and therefore we linearly interpolated the pupil-sizes and the three gaze positions (x, y, and d ($= \sqrt{x^2 + y^2}$)) before and after the blink events.

To minimize confounding effects from gaze position on pupil-size measurements, we processed the blink-free samples of pupil-size and three gaze positions time series by linear detrending, band-pass filtering (0.01Hz to 4Hz cut-off frequency with a Butterworth filter), and resampling to 10Hz. The resampled time series of pupil-size was then orthogonalized from the three resampled gaze positions up to their fourth powers (total 12 regressors) to extract any confounding in the pupil-size originating from the gaze position[35]. The orthogonalized pupil-size time series was then standardized by subtracting the mean and dividing the standard deviation of the time series. The pupil-sizes of the eyes were averaged, and trials were epoched and baseline corrected by subtracting the baseline pupil-size averaged across 0ms to 500ms from the stimulus onset. We chose this baseline time window because we assumed that the decision-related pupil signal would be initiated between -200ms to 300ms from the stimulus onset and because the latency of the empirical responses was around 200ms[46]. Finally, the baseline corrected pupil-sizes were aligned by the stimulus onset or the choice following previous studies[15,47].

Literature

1 Benjamin, A. S., Diaz, M. & Wee, S. Signal detection with criterion noise: Applications to recognition memory. *Psychological review* **116**, 84 (2009).

2 Lages, M. & Treisman, M. A criterion setting theory of discrimination learning that accounts for anisotropies and context effects. *Seeing and perceiving* **23**, 401-434 (2010).

3 Morgan, M., Watamaniuk, S. & McKee, S. The use of an implicit standard for measuring discrimination thresholds. *Vision research* **40**, 2341-2349 (2000).

4 Norton, E. H., Fleming, S. M., Daw, N. D. & Landy, M. S. Suboptimal criterion learning in static and dynamic environments. *PLoS computational biology* **13**, e1005304 (2017).

5 Raviv, O., Lieder, I., Loewenstein, Y. & Ahissar, M. Contradictory behavioral biases result from the influence of past stimuli on perception. *PLOS Comput Biol* **10**, e1003948 (2014).

6 Hachen, I., Reinartz, S., Brasselet, R., Stroligo, A. & Diamond, M. Dynamics of history-dependent perceptual judgment. *Nature communications* **12**, 1-15 (2021).

7 Lages, M. & Treisman, M. Spatial frequency discrimination: visual long-term memory or criterion setting? *Vision research* **38**, 557-572 (1998).

8 Treisman, M. & Williams, T. C. A theory of criterion setting with an application to sequential dependencies. *Psychological Review* **91**, 68 (1984).

9 Lee, H., Lee, H.-J., Choe, K. W. & Lee, S.-H. Neural evidence for boundary updating as the source of the repulsive bias in classification. *bioRxiv*, 2023.2001. 2011.523692 (2023).

10 Bosch, E., Fritsche, M., Ehinger, B. V. & de Lange, F. P. Opposite effects of choice history and evidence history resolve a paradox of sequential choice bias. *Journal of vision* **20**, 9-9 (2020).

11 Behrens, T. E., Woolrich, M. W., Walton, M. E. & Rushworth, M. F. Learning the value of information in an uncertain world. *Nature neuroscience* **10**, 1214 (2007).

12 Drugowitsch, J., Mendonça, A. G., Mainen, Z. F. & Pouget, A. Learning optimal decisions with confidence. *Proceedings of the National Academy of Sciences* **116**, 24872-24880 (2019).

13 Shenhav, A., Cohen, J. D. & Botvinick, M. M. Dorsal anterior cingulate cortex and the value of control. *Nature neuroscience* **19**, 1286-1291 (2016).

14 Fietz, J. *et al.* Pupillometry tracks cognitive load and salience network activity in a working memory functional magnetic resonance imaging task. *Human Brain Mapping* **43**, 665-680 (2022).

15 Urai, A. E., Braun, A. & Donner, T. H. Pupil-linked arousal is driven by decision uncertainty and alters serial choice bias. *Nature communications* **8**, 14637 (2017).

16 Grinband, J., Hirsch, J. & Ferrera, V. P. A neural representation of categorization uncertainty in the human brain. *Neuron* **49**, 757-763 (2006).

17 Braun, A., Urai, A. E. & Donner, T. H. Adaptive history biases result from confidence-weighted accumulation of past choices. *Journal of Neuroscience* **38**, 2418-2429 (2018).

18 Brown, J. W. & Braver, T. S. Learned predictions of error likelihood in the anterior cingulate cortex. *Science* **307**, 1118-1121 (2005).

19 Buracas, G. T. & Boynton, G. M. Efficient design of event-related fMRI experiments using M-sequences. *Neuroimage* **16**, 801-813 (2002).

20 Sanders, J. I., Hangya, B. & Kepecs, A. Signatures of a statistical computation in the human sense of confidence. *Neuron* **90**, 499-506 (2016).

21 Kepecs, A., Uchida, N., Zariwala, H. A. & Mainen, Z. F. Neural correlates, computation and behavioural impact of decision confidence. *Nature* **455**, 227 (2008). https://doi.org:10.1038/nature07200
https://www.nature.com/articles/nature07200#supplementary-information

22 Shenhav, A., Straccia, M. A., Cohen, J. D. & Botvinick, M. M. Anterior cingulate engagement in a foraging context reflects choice difficulty, not foraging value. *Nature neuroscience* **17**, 1249 (2014).

23 Cho, R. Y. *et al.* Mechanisms underlying dependencies of performance on stimulus history in a two-alternative forced-choice task. *Cognitive, Affective, & Behavioral Neuroscience* **2**, 283-299 (2002).
24 Kristjánsson, Á. & Campana, G. Where perception meets memory: A review of repetition priming in visual search tasks. *Attention, Perception, & Psychophysics* **72**, 5-18 (2010).
25 Galluzzi, F., Benedetto, A., Cicchini, G. M. & Burr, D. C. Visual priming and serial dependence are mediated by separate mechanisms. *Journal of Vision* **22**, 1-1 (2022).
26 Urai, A. E., De Gee, J. W., Tsetsos, K. & Donner, T. H. Choice history biases subsequent evidence accumulation. *Elife* **8**, e46331 (2019).
27 Rahnev, D., Koizumi, A., McCurdy, L. Y., D'Esposito, M. & Lau, H. Confidence leak in perceptual decision making. *Psychological science* **26**, 1664-1680 (2015).
28 Jentzsch, I. & Dudschig, C. Short article: Why do we slow down after an error? Mechanisms underlying the effects of posterror slowing. *Quarterly Journal of Experimental Psychology* **62**, 209-218 (2009).
29 Seeley, W. W. The salience network: a neural system for perceiving and responding to homeostatic demands. *Journal of Neuroscience* **39**, 9878-9882 (2019).
30 Shekhar, M. & Rahnev, D. Sources of metacognitive inefficiency. *Trends in Cognitive Sciences* **25**, 12-23 (2021).
31 McGuire, J. T., Nassar, M. R., Gold, J. I. & Kable, J. W. Functionally dissociable influences on learning rate in a dynamic environment. *Neuron* **84**, 870-881 (2014).
32 Lak, A. *et al.* Reinforcement biases subsequent perceptual decisions when confidence is low, a widespread behavioral phenomenon. *ELife* **9**, e49834 (2020).
33 Fritsche, M., Mostert, P. & de Lange, F. P. Opposite effects of recent history on perception and decision. *Current Biology* **27**, 590-595 (2017).
34 Fründ, I., Wichmann, F. A. & Macke, J. H. Quantifying the effect of intertrial dependence on perceptual decisions. *Journal of vision* **14**, 9-9 (2014).
35 Choe, K. W., Blake, R. & Lee, S.-H. Pupil size dynamics during fixation impact the accuracy and precision of video-based gaze estimation. *Vision research* **118**, 48-59 (2016).
36 Choe, K. W., Blake, R. & Lee, S.-H. Dissociation between neural signatures of stimulus and choice in population activity of human V1 during perceptual decision-making. *Journal of Neuroscience* **34**, 2725-2743 (2014).
37 Lee, H.-J., Lee, H., Lim, C. Y., Rhim, I. & Lee, S.-H. What humans learn from corrective feedback for perceptual decision-making. *bioRxiv*, 2023.2001. 2011.523567 (2023).
38 Borcard, D., Legendre, P. & Drapeau, P. Partialling out the spatial component of ecological variation. *Ecology* **73**, 1045-1055 (1992).
39 Perquin, M. N., Heed, T. & Kayser, C. Variance (un) explained: Experimental conditions and temporal dependencies explain similarly small proportions of reaction time variability in perceptual and cognitive tasks. *bioRxiv*, 2022.2012. 2022.521656 (2022).
40 Nestares, O. & Heeger, D. J. Robust multiresolution alignment of MRI brain volumes. *Magnetic Resonance in Medicine: An Official Journal of the International Society for Magnetic Resonance in Medicine* **43**, 705-715 (2000).
41 Ashburner, J. A fast diffeomorphic image registration algorithm. *Neuroimage* **38**, 95-113 (2007).
42 Friston, K. J., Williams, S., Howard, R., Frackowiak, R. S. & Turner, R. Movement-related effects in fMRI time-series. *Magnetic resonance in medicine* **35**, 346-355 (1996).
43 Jenkinson, M., Bannister, P., Brady, M. & Smith, S. Improved optimization for the robust and accurate linear registration and motion correction of brain images. *Neuroimage* **17**, 825-841 (2002).
44 Cox, R. W. AFNI: software for analysis and visualization of functional magnetic resonance neuroimages. *Computers and Biomedical research* **29**, 162-173 (1996).

45 Benjamini, Y. & Hochberg, Y. Controlling the false discovery rate: a practical and powerful approach to multiple testing. *Journal of the royal statistical society. Series B (Methodological)*, 289-300 (1995).

46 Korn, C. W. & Bach, D. R. A solid frame for the window on cognition: Modeling event-related pupil responses. *Journal of vision* **16**, 28-28 (2016).

47 de Gee, J. W., Knapen, T. & Donner, T. H. Decision-related pupil dilation reflects upcoming choice and individual bias. *Proceedings of the National Academy of Sciences* **111**, E618-E625 (2014).